IOSR Journal Of Applied Physics (IOSR-JAP)
e-ISSN: 2278-4861.Volume 16, Issue 4 Ser. 1 (July. – August. 2024), PP 57-64
www.Iosrjournals.Org

Influence Of RE-Sm^{3+} Ion Doping On The Morphological And Structural Study Of Cu-Mg Nano-Ferrite Made Using The Citrate Sol-Gel Auto-Combustion Technique

P. Ramesh[1], G. Vinod[2], K. Rajashekhar[3], Noha Ahmed Elayah[4], B. Sreematha[5], G. Sunitha[6], J. Laxman Naik[7*]

[1,4,7*]*Department Of Physics, Osmania University, Hyderabad, Telangana, India-500007.*
[2,6]*Department Of H&S (Physics), Teegala Krishna Reddy Engineering College TKREC, Medbowli, Meerpet, Hyderabad - 500097, Telangana.*
[3]*Department Of Physics, Kamala Institute Of Technology And Science, Huzurabad 505468, Telangana, India.*
[5]*Department Of Physics, Telangana University, Nizamabad – 503322, India*
**Corresponding Author: laxmannaikj@gmail.com*

Abstract:
The citrate sol-gel auto-combustion method was used in this study to synthesize spinel ferrites, which have the general formula $Cu_{0.7}Mg_{0.3}Fe_{2-x}Sm_xO_4$ (x=0.000–0.020). X-ray diffraction spectroscopy was used to confirm the development of the cubic spinel phase and structural modifications caused by the substitution of Sm^{3+}. P-XRD spectra show that the range of crystallite sizes is 35.84-34.26 nm. Field emission scanning and transmission electron microscopy were used to study these ferrites' surface morphology and microstructure. Fourier transforms infrared spectra observed that the metal-oxygen (M-O) bonds in Cu-Mg ferrite samples were systematically changed by Sm^{3+} doping.

Keyword*: Sm^{3+} doped Cu-Mg Ferrites; PXRD; FESEM; FTIR*

Date of Submission: 29-07-2024 Date of Acceptance: 09-08-2024

I. Introduction

The importance of studying soft ferrites with cubic spinel structures has grown dramatically. These soft ferrites, with their diverse applications in memory devices, computer components, microwave-absorbing materials, cancer treatment, filters and satellite communication, magnetic resonance imaging, magnet recording medium, ferrofluids, transformer cores, and antenna rods, present a fascinating field of study. The structural, optical, and electrical properties of soft ferrites provide the necessary information for the specific uses of these materials. Assuming A and B to be metallic cations, the standard equation for spinel ferrite is AB2O4. Two distinct crystallographic sites where metallic cations have been identified are octahedral (B-site) and tetrahedral (A-site). The cations of both positions are octahedral and tetrahedral, respectively, which coordinate oxygen atoms. The cubic closed oxygen ion configuration that constitutes up the spinel ferrite unit cell has thirty-two octahedral (B-site) and sixty-four tetrahedral (A-site) locations. A combined total of 8-A sites and 16-B sites are occupied by metal cations [4–6]. The preparation techniques, annealing temperature, chemical composition, and tetrahedral octahedral cationic dispersion significantly affect spinel ferrite's magnetic and dielectric characteristics. However, some of the most significant magnetic oxides replaced Sm3+ substituted soft ferrites because of their high Curie temperature, high DC electrical resistivity, and environmental stability [7,8]. Microwave devices, like spinel ferrites, are usually employed to regulate transmission route, frequency, and amplitude. Various researchers have explained the doping of rare earth elements in spinel ferrites. Microwave devices, like spinel ferrites, are usually employed to regulate transmission route, frequency, and amplitude [9] An increasing number of studies have focused on soft ferrites regarding cubic spinel structures. Soft ferrites identify applications in many fields, including filtering and satellite communication, magnetic resonance imaging, computer chips, memory devices, microwave-absorbing materials, chemotherapy for cancer, ferrofluids, transformer cores, and antenna rods. However, on the other hand, since 4f electrons become restricted to a region of rare earth (RE3+), elements have high magneto-crystalline anisotropy, high magnetostriction, and elevated magnetic moments at low temperatures [10–13]. Therefore, doping nano-ferrites using trace amounts of REs can enhance their magnetic properties. Because of its great uniformity and purity, sol-gel auto combustion is an adaptable and appropriate method. In the present study, the Mg0.5Cu0.25Fe2–xSmxO4 (0.00 ~ x 0.020) soft ferrites (MCSF-soft ferrites) were synthesized using the sole

gel auto-combustion technique, and their structural morphological, compositional, vibrational, optical, electrical, dielectric, and magnetic properties were examined, promising exciting new insights and potential applications.

II. Materials And Methods

Materials

In the present study, Cu0.7Mg0.3Fe2-xSmxO4 nano-ferrites were synthesized using magnesium nitrate hexahydrate [Mg (NO3)2 6H2O] (99.9% Merck), copper nitrate hexahydrate [Cu (NO3)2 6H2O] (99.9% Merck), samarium nitrate hexahydrate [Sm (NO3)365H2O] (Sigma-Aldrich), iron-nitrate nonahydrate [Fe (NO3)3 9H2O] (99% SRL chemical, India), and magnesium, copper, manganese, and iron, respectively. Before doing any additional purification, ferrite was synthesized using the salts and reagents, all of which were obtained through Sigma-Aldrich chemicals.

Method to synthesize CMSF nano-ferrite preparation

$Cu_{0.7}Mg_{0.3}Sm_xFe_{2-x}O_4$ samples (x = 0.00, 0.004, 0.008 0.012, 0.016 and 0.020) specifically $Cu_{0.7}Mg_{0.3}Fe_2O_4$(CMSF-O), $Cu_{0.7}Mg_{0.3}Sm_{0.004}Fe_{1.996}O_4$ (CMSF-1), $Cu_{0.7}Mg_{0.3}Sm_{0.008}Fe_{1.992}O_4$ (CMSF-2), $Cu_{0.7}Mg_{0.3}Sm_{0.012}Fe_{1.988}O_4$ (CMSF-3), $Cu_{0.7}Mg_{0.3}Sm_{0.016}Fe_{1.984}O_4$ (CMSF-4) and $Cu_{0.7}Mg_{0.3}Sm_{0.020}Fe_{1.980}O_4$ (CMSF-5), they were produced through employing the citrate technique. Based on stoichiometric estimations, magnesium, copper, iron, and Samarium nitrates were employed. The burning agent in consideration was citric acid. First, distilled water dissolved the nitrates and citric acid in a 1:3 molar ratio. The nitrates and citric acid were individually dissolved in distilled water using magnetic stirring. Drop by drop, ammonia solution was added to the mixture to maintain a pH of 7. After constantly agitating the mixture for almost an hour, a dry gel was produced at 373 K. Subsequently, the gel became a dry gel, the stirring was stopped, and the gel became exclusively heated, allowing the auto-combustion procedure to produce the final products. The prepared components were ground for thirty minutes to reach their ideal state. After the powders sintered for 4 hours at 650 °C, the samples were reground for 15 to 20 minutes, which decreased the material's porosity while increasing its strength and integrity. The resulting powder was then subjected to 1500 MPa of pressure to compress into pellets. The pellets and powder were sintered for 4 hours at 650 °*C*. The entire process is depicted in Figure 1. The produced ferrites were analyzed using various methods.

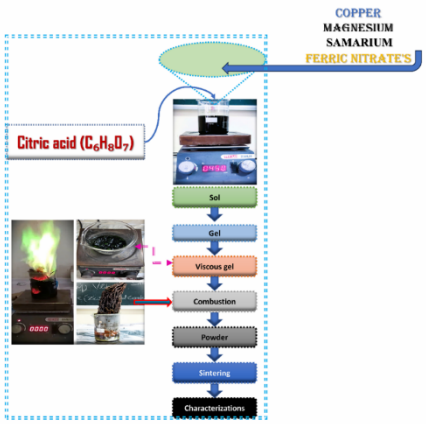

Fig. 1. The flow chart of citrate gel auto combustion method for the preparation of $Cu_{0.7}Mg_{0.3}Fe_{2-x}Sm_xO_4$ (x = 0.000 (CMSF-0), 0.004 CMSF-1, 0.008 CMSF-2, 0.012 CMSF-3, 0.016 CMSF-4 and 0.020 5) nano ferrites.

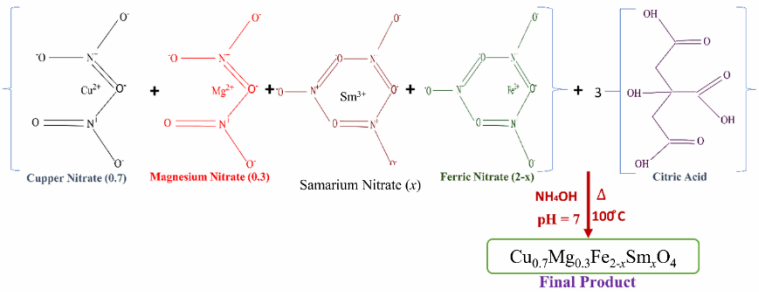

Fig. 1. (b) Schematic of the mechanism of $Cu_{0.7}Mg_{0.3}Fe_{2-x}Sm_xO_4$ nano-ferrite synthesis.

Structure characterization of CMSF nano-ferrite

X-ray diffraction (XRD) was employed to obtain crystal configuration and smoothness data and determine crystal structure and phase composition. The morphological features of the produced nanoparticles were examined using scanning electron microscopy (FESEM). FTIR Spectroscopy was used to identify the surface qualitative examination of developed ferrite nanoparticles as well as their cation distribution at interstitial A- and B-sites.

III. Results And Discussion

P-XRD analysis of CMSF nano-ferrite

Fig. 2 displays the powder patterns obtained from XRD of $Cu_{0.7}Mg_{0.3}Sm_xFe_{2-x}O_4$ samples (x = 0.00, 0.004, 0.008 0.012, 0.016 and 0.020) after being annealed at 700 degrees Celsius. The 700-degree samples' patterns indicate a single-phase, extremely pure spinel crystal structure [1,2]. The powder that was calcined at 700°C exhibited diffraction peaks at 2θ values of 18.24°, 30.32°, 35.71°, 37.55°, 43.56°, 53.73°, 57.84° and 62.96°. The planes (111), (220), (311), (222), (400), (422), and (511) accordingly corresponded to these peaks. The peaks in question corresponded with ICDD data card number #01-080-6487 for CuMgFe2O4. The P-XRD data and values were utilized to estimate the different structural parameters employing the following relations [3–6]: The results of all the structural parameters obtained are recorded in Table 1.

(1)

where β is the full width at half maxima, θ is Bragg's diffraction angle, and λ is the X-ray wavelength.

(2)

(3)

This lattice constant value was also used to determine a given angle's specific plane (h k l). The interplanar distances (d) between the computed and observed values coincide reasonably well.

(4)

where a denotes the lattice constant, and V represents the unit cell volume.

(5)

(6)

(7)

(8)

(9)

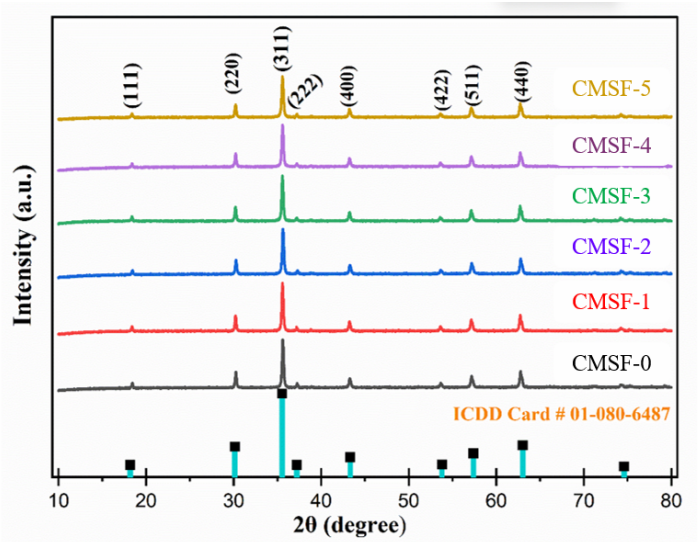

Fig. 2 shows the P-XRD patterns of Sm^{3+}-doped (CMSF-0- CMSF-5) nano ferrites.

The average crystallite size of the samples varied from 35.84 to 34.26nm. According to CMSF-0 to CMSF-5, the tensile strain decreased as the Sm^{3+} concentration rose. Sm^{3+} ions, larger than Fe^{3+} ions in the samples, led to the assumption that the tensile strain would rise with Sm^{3+} concentration. Improving the crystallite size during the sol-gel formation process requires the nucleation process. Concentrated heating of the surrounding ions occurs upon the addition of Sm^{3+} cations. This could be because of the differing ionic radii of the ions Fe^{3+} (0.645) and Sm^{3+} (0.958), which induce a temperature difference in the solution. An Ostwald mechanism causes the size expansion of the crystallite [7–9]. The values of the lattice constant increased as the concentration of Sm^{3+} ions increased, as Table 1 illustrates. Sm^{3+} (0.0858 nm) and Fe^{3+} (0.0645 nm) ionic radii

alterations cause the increasing value in the lattice constant. These results are good. As solid solutions develop within the separation range, Table 1, recorded P-XRD data, demonstrates that the lattice parameters and substituent amount show a roughly linear relationship. This is the behavior of homogeneous alloys according to Vegard's law. More often than not, stoichiometric fluctuations and the defects or vacancies they cause cause a slight separation outside of Vegard's law. agreement with the literature-published findings. By using Sm^{3+} ions to replace the smaller Fe^{3+} ions, the ac increased from 8.3782 to 8.3829 Å, and the cell volume increased from 588.1038 to 591.4717 $Å^3$ [10]. Table 1, recorded P-XRD results, shows that the lattice parameters and substituent amount exhibit an approximately linear relationship when solid solutions form within the separation range. This is following the way uniform alloys that follow Vegard's law behave. The presence of stoichiometric variations and the faults or vacancies they generate typically result in a minor separation beyond Vegard's law [11]. Equations (7), (8), and (9), respectively, were used to obtain the bulk density (dB), x-ray density (dx), and porosity (P%) for the CMSF series of samples. The results are shown in Table 1 as a function of Sm^{3+} content. The fact that the d*x* and d_B show a comparable pattern of decline with increasing Sm^{3+} concentration lends credence to the manufactured powder density. The observed density decreases result from molecular weight loss in the investigated materials. Usually, the d_B values are less than the measurements of the X-ray density. However, the Sm^{3+}-substituted Cu-Mg iron oxide nanoparticles' component-related bulk density value found the opposite tendency [12,13]. Table 6.1 shows that L_A and L_B increase predictably when crystallite size increases. This better-hopping length (L_A and L_B) can be used to predict higher bond length (A–O/B–0), which could be another factor contributing to the increased cell volume. In addition, the LA value is greater than the L_B value, indicating a smaller chance of electron hopping among cations at A and B sites compared to B and B sites. Table 1 clarifies that the concentration of Sm^{3+} causes a composition-dependent fluctuation in bulk density (d_B) and X-ray density (d_x). The development of the molar weights of the Cu-Mg ferrites nanomaterials samples substituted with Sm^{3+} could have explained the increase in X-ray density values as Sm^{3+} ions were added. It has been observed that adding Sm^{3+} content (CMSF-0 to CMSF-5) increases the porosity of the samples from the CMSF-0 to CMSF-5 series. The porosity results for the CMSF samples were between 33 to 49%. Changes in bulk and X-ray densities following the use of the Sm^{3+} cause a decrease in porosity, which could result from vacancies brought on by variations in ionic radii [14].

Table 1. Structural parameter crystallite size (D), lattice parameter (a), Volume (V), X-ray density (d_x), bulk density (d_B), and percentage porosity (P%) for the synthesized $Cu_{0.7}Mg_{0.3}Sm_xFe_{2-x}O_4$ CMSF-0, CMSF-1, CMSF-2, CMSF-3, CMSF-4, and CMSF-5 ferrite nanoparticles.

Composition	*D* (nm)	a ( )	V ( )^3	Hopping lengths (A-site and B-site)		d_x (gm/cm^3)	d_B (gm/cm^3)	P (%)
				L_A ( )	L_B ( )			
CMSF-0	35.84	8.3782	588.1038	3.6278	2.9621	5.137	2.824	49.98
CMSF-1	35.81	8.4127	588.5833	3.6428	2.9743	5.3261	3.3012	38.02
CMSF-2	35.41	8.4027	589.0634	3.6385	2.9708	5.3841	3.3503	37.77
CMSF-3	35.33	8.4035	589.544	3.6388	2.9711	5.4221	3.4655	36.09
CMSF-4	34.61	8.3830	590.5068	3.6299	2.9638	5.5016	3.5576	35.34
CMSF-5	34.26	8.3829	591.4717	3.6299	2.9638	5.5414	3.6917	33.38

FE-SEM analysis of CMSF nano-ferrite

The surface shape of the identified Sm^{3+}-doped $Cu_{0.7}Mg_{0.3}Sm_xFe_{2-x}O_4$ (CMSF-0 to CMSF-5) ferrite NPs is displayed in Fig. 3. The FE-SEM micrographs show morphology toward aggregation that is berry-like, non-uniform, and almost spherical. The nanoparticles tend to aggregate due to their strong surface energy and mutual magnetic interactions, comparable with the FESEM investigation [15,16]. According to Fig. 3, there are high pores and voids with a high dimension present in CMSF-0. In addition, more significant cracks and an average morphology were seen. Nonetheless, the morphology is significantly altered from CMSF-0 to CMSF-5. Sm^{3+} addition to $Cu_{0.7}Mg_{0.3}Sm_xFe_{2-x}O_4$ ferrites has a significant impact on the surface morphology. Sm-CMSF-0 to CMSF-5 significantly modifies the inter and intra-granular structure of CMSF-0. More massive grain sizes are seen in all Sm-substituted samples than their unsubstituted associates. As a sintering representative for the Sm-substituted materials, Sm is thought to be responsible for the observed phenomenon. Employing the Image J program to approximate the particle size distribution with a Lorentz function, the observed grain size findings from FE-SEM micrographs for CMSF-0 to CMSF-5 are 59.9-45.15 nm, correspondingly.

Compositional study of CMSF nano-ferrite

The EDS patterns of every bulk ferrite $Cu_{0.7}Mg_{0.3}Sm_xFe_{2-x}O_4$ (CMSF-0 to CMSF-5) doped with Sm^{3+} are displayed in Fig. 4. By identifying the chemical nature of the elements existing throughout the solid's surface to

its core areas, the EDS spectra confirm the homogeneity of the samples that are being investigated. As shown in Fig. 4, predicted peaks for metals Cu, Mg, Fe, O, and Sm verify the fundamental composition of the produced nanocatalysts. Remarkably, the strength of the Sm^{3+} peak increases with increasing Sm-doping in the Cu-Mg ferrites (Fig.4).

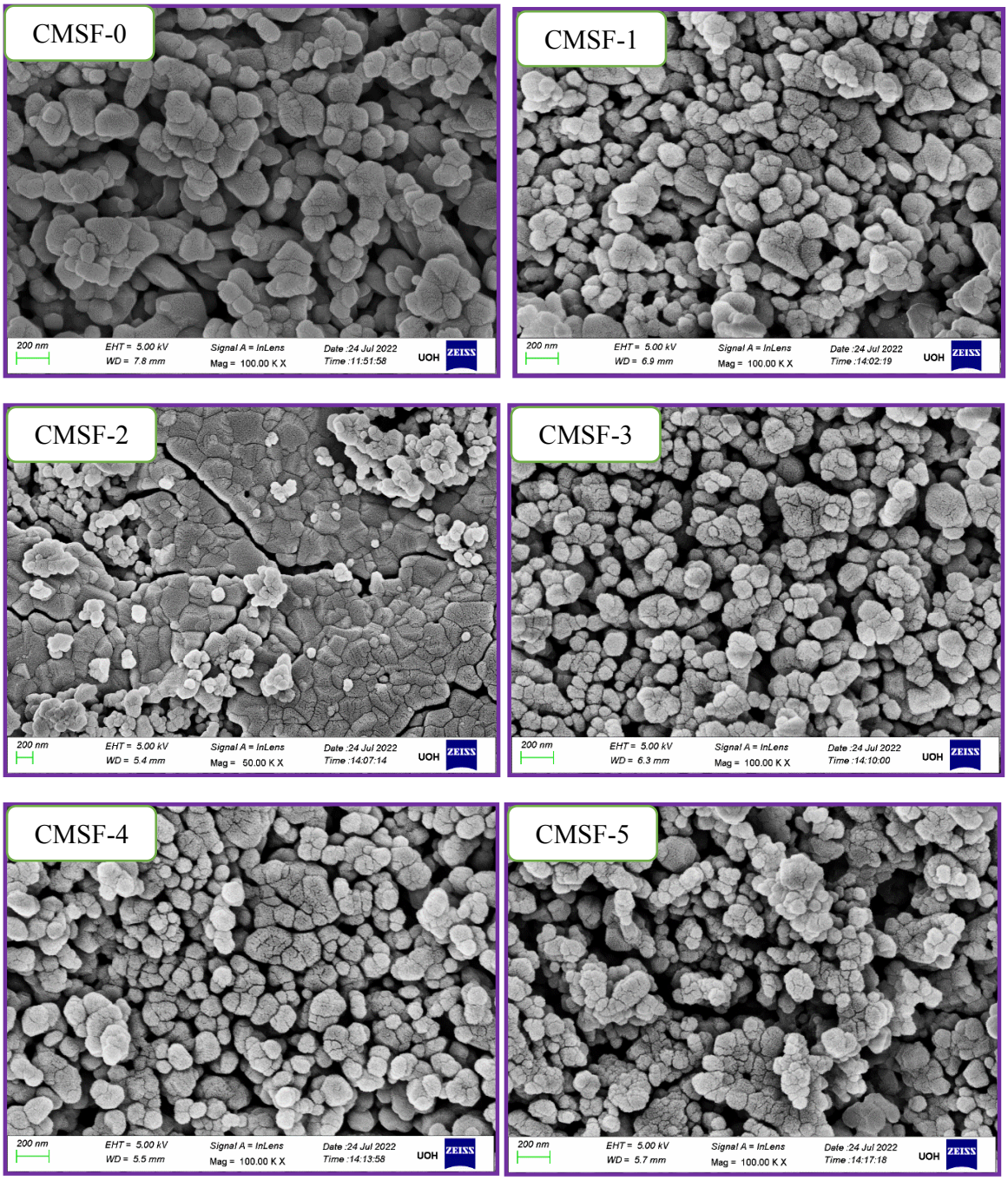

Fig. 3. FESEM photographs of pristine (CMSF-0) and Sm^{3+}-doped (CMSF-1- CMSF-5) nano-ferrites.

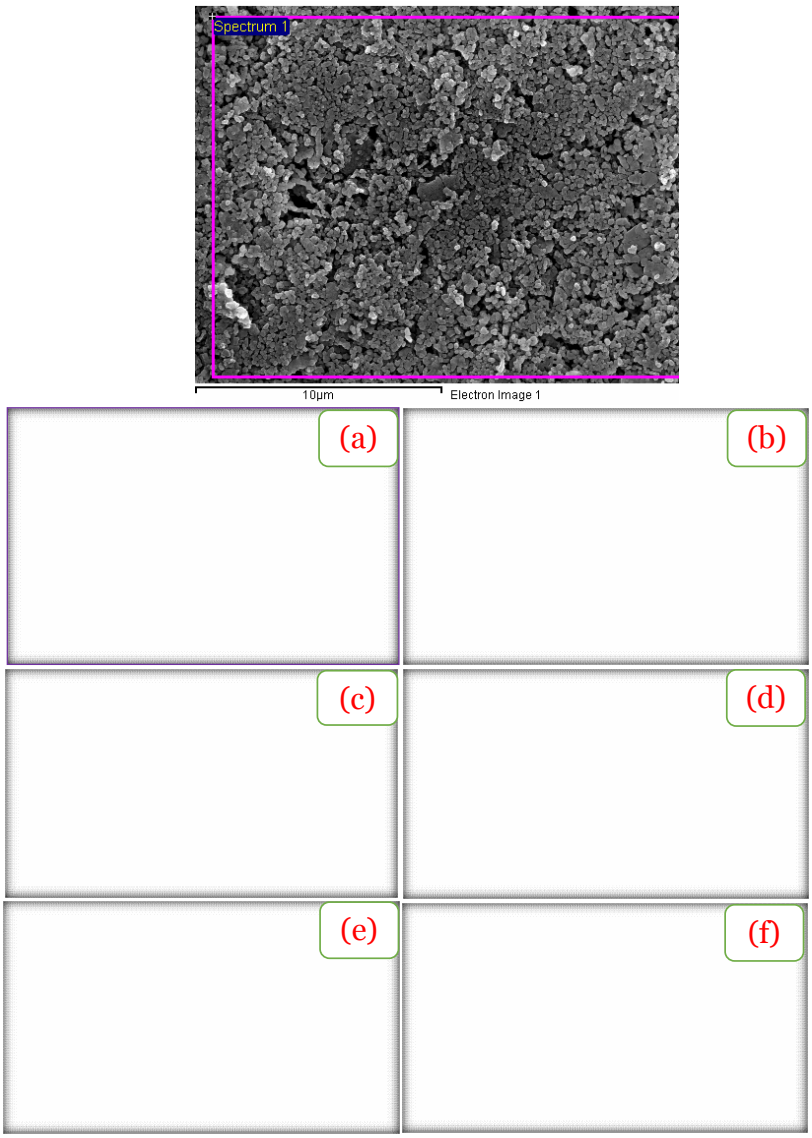

Fig. 4. EDX photographs of pristine (CMSF-0) and Sm^{3+}-doped (CMSF-1- CMSF-5) nano ferrites.

Infrared spectroscopy (FTIR) analysis of CMSF nano-ferrite

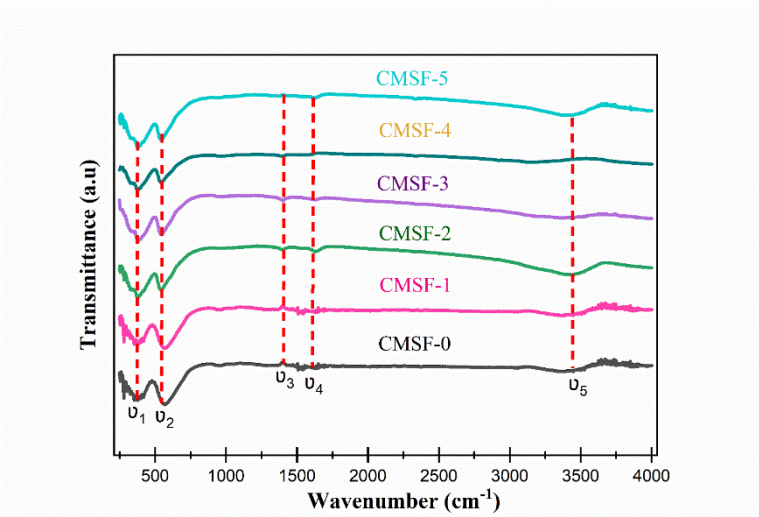

Fig. 5. *FTIR transmission spectra of $Cu_{0.7}Mg_{0.3}Fe_{2-x}Sm_xO_4$ (x= CMSF-0 to CMSF-5) ferrite nanoparticles.*

FTIR is an effective method for estimating ferrites' thermodynamic state and elastic characteristics. As a result, a single spinel cubic structure was verified in all of the samples under investigation when FTIR spectra were acquired at RT with a wavenumber variation ranging from 350 to 4000 cm^{-1}. All examined samples' IR spectra are displayed in Fig. 5. This data shows two firm absorption peaks, designated as υ_1 and υ_2, respectively, at 587 cm-^{1} and 416 cm^{-1}. Generally, the oxygen motion at the tetrahedral site (A-site) is attributed to the absorption band at around 587 cm^{-1}. The absorption band at 1085 cm^{-1} indicates the C–N vibration. Moreover, the band at 1399 cm^{-1} is due to trapped nitrates. The absorption peak nA continues to be broad upon increasing the substitution of Sm^{3+} at Fe^{3+} ions. The reason is that the distance between Fe–O bonds at the octahedral site is highly affected when Sm^{3+}, with its larger ionic radius and atomic weight, sits at the place of Fe^{3+}. Furthermore, the absence of any shoulder at v_B confirms the presence of Fe^{2+} striking out of the octahedral site. The slight shift in absorption bands at υ_1 and υ_2 to the lower side indicates the perturbation in the Fe^{2+}-O^{2-} bond that occurred for Sm^{3+} substitution. The C–the absorption band indicates N vibration at 1085 cm^{-1}. Additionally, trapped nitrates cause the band to be around 1421 cm^{-1}. As the substitution of Sm^{3+} at Fe^{3+} ions increases, the absorption of all peaks remains broad. The rationale is that when Sm^{3+}, with its greater ionic radius and atomic weight, sits in place of Fe^{3+}, it significantly affects the distance between Fe-O bonds at the octahedral site. Moreover, Fe^{2+} striking out of the octahedral site is confirmed by the absence of a shoulder at v_B. The Fe^{2+}-O^2 bond disturbance from the Sm^{3+} substitution is indicated by the slight shift of the absorption bands at υ_1 and υ_2 to the higher side. Fig 5 summarizes the acquired FTIR data for our examined materials. The vibrational modes linked to O-H (and potentially C-H/CC) functional groups can be attributed to the absorption bands detected at 1614-1624 cm^{-1} [30]. These modes show the typical cycles of H-O-H bonds and bridging water. Furthermore, the absorption band at 3455-3458 cm^{-1} is linked to the O-H stretching vibration, which signifies the creation of hydrogen bonds between hydroxyl groups. This finding implies that the samples include either absorbed or free water [17,18].

IV. Conclusion

Spinel nano-ferrites $Cu_{0.7}Mg_{0.3}Sm_xFe_{2-x}O_4$ (CMSF-0 to CMSF-5) were synthesized using the sol-gel auto-combustion process and annealed at 700 ^{0}C. The sample's revelation explained the cubic phase's crystallization at roughly 500 ^{0}C after it was annealed at 700 ^{0}C. FE-SEM images were used to study the morphology of spinel nanoparticles. The energy-dispersive X-ray method is used to ensure the presence of elements in the Sm-doped $CuMgFe_2O_4$ Nanoparticles. The band at approximately 400-600 cm^{-1}, corresponding to the stretching vibration of the tetrahedral site (Fe^{3+}-O^{2-}) and octahedral site (Cu-Mg^{2+} -O^{2-}), respectively, validates the structure of the copper magnesium spinel ferrites.

References

[1]. E. Ateia, M.A. Ahmed, R.M. Ghouniem, Electrical Properties And Initial Permeability Of Cu–Mg Ferrites, Solid State Sci 31 (2014) 99–106. Https://Doi.Org/10.1016/J.Solidstatesciences.2014.03.002.

[2]. H. Zhang, V. Malik, S. Mallapragada, M. Akinc, Synthesis And Characterization Of Gd-Doped Magnetite Nanoparticles, J Magn Magn Mater 423 (2017) 386–394. Https://Doi.Org/10.1016/J.Jmmm.2016.10.005.

[3]. M.A. Almessiere, S. Güner, H. Gungunes, M. Sertkol, Y. Slimani, R. Badar, S. Akhtar, S.E. Shirsath, A. Baykal, Structural, Magnetic, And Mossbauer Parameters' Evaluation Of Sonochemically Synthesized Rare Earth Er3+And Y3+Ions-Substituted Manganese-Zinc Nanospinel Ferrites, Acs Omega 6 (2021) 22429–22438. Https://Doi.Org/10.1021/Acsomega.1c03416/Asset/Images/Large/Ao1c03416_0012.Jpeg.

[4]. A.R. Liandi, A.H. Cahyana, A.J.F. Kusumah, A. Lupitasari, D.N. Alfariza, R. Nuraini, R.W. Sari, F.C. Kusumasari, Recent Trends Of Spinel Ferrites (Mfe2o4: Mn, Co, Ni, Cu, Zn) Applications As An Environmentally Friendly Catalyst In Multicomponent Reactions: A Review, Case Studies In Chemical And Environmental Engineering 7 (2023) 100303. Https://Doi.Org/10.1016/J.Cscee.2023.100303.

[5]. M. Kazemi, Based On Mfe2o4 (M=Co, Cu, And Ni): Magnetically Recoverable Nanocatalysts In Synthesis Of Heterocyclic Structural Scaffolds, Synth Commun 50 (2020) 1899–1935. Https://Doi.Org/10.1080/00397911.2020.1723109.

[6]. J.M. Gonçalves, L. V. De Faria, A.B. Nascimento, R.L. Germscheidt, S. Patra, L.P. Hernández-Saravia, J.A. Bonacin, R.A.A. Munoz, L. Angnes, Sensing Performances Of Spinel Ferrites Mfe2o4 (M = Mg, Ni, Co, Mn, Cu And Zn) Based Electrochemical Sensors: A Review, Anal Chim Acta 1233 (2022) 340362. Https://Doi.Org/10.1016/J.Aca.2022.340362.

[7]. A. Balamurugan, R.S. Priya, P. Chaudhary, E.R. Kumar, T. Indumathi, C. Srinivas, B.C. Yadav, D.L. Sastry, Natural Fuel Assisted Synthesis Of Mg–Cu Ferrite Nanoparticles: Evaluation Of Structural, Dielectric, Magnetic And Humidity Sensing Properties, Ceram Int 48 (2022) 4874–4885. Https://Doi.Org/10.1016/J.Ceramint.2021.11.024.

[8]. A.B. Gadkari, T.J. Shinde, P.N. Vasambekar, Influence Of Rare Earth Ion (Y 3+) On The Magnetic And Dc Electrical Properties Of High Density Nanocrystalline Mg-Cd Ferrites, (N.D.). Https://Doi.Org/10.1016/J.Materresbull.2012.11.009.

[9]. R. Qindeel, N.H. Alonizan, E.A. Alghamdi, M.A. Awad, Synthesis And Characterization Of Spinel Ferrites For Microwave Devices, J Solgel Sci Technol 97 (2021) 593–599. Https://Doi.Org/10.1007/S10971-021-05470-9/Figures/9.

[10]. L. Shao, A. Sun, Y. Zhang, L. Yu, N. Suo, Z. Zuo, Comparative Study On The Structure And Magnetic Properties Of Ni-Mg-Co Ferrite Doped With Al And Rare Earth Elements, Journal Of Materials Science: Materials In Electronics 32 (2021) 5339–5352. Https://Doi.Org/10.1007/S10854-020-05161-1/Figures/7.

[11]. X. Wu, S. Yan, W. Liu, Z. Feng, Y. Chen, V.G. Harris, Influence Of Particle Size On The Magnetic Spectrum Of Nicuzn Ferrites For Electromagnetic Shielding Applications, J Magn Magn Mater 401 (2016) 1093–1096. Https://Doi.Org/10.1016/J.Jmmm.2015.10.129.

[12]. C. Stergiou, Magnetic, Dielectric And Microwave Absorption Properties Of Rare Earth Doped Ni–Co And Ni–Co–Zn Spinel Ferrites, J Magn Magn Mater 426 (2017) 629–635. Https://Doi.Org/10.1016/J.Jmmm.2016.11.001.

[13]. M.N. Akhtar, H.A. Siddiqa, M.S. Nazir, M.A. Khan, Preparations And Tailoring Of Structural, Magnetic Properties Of Rare Earths (Res) Doped Nanoferrites For Microwave High Frequency Applications, Ceram Int 46 (2020) 26521–26529. Https://Doi.Org/10.1016/J.Ceramint.2020.07.118.
[14]. M.I.U. Haq, A. Ur Rehman, M. Asghar, M.A.U. Nabi, N. Amin, S. Tahir, M.I. Arshad, Influence Of Ce3+ And La3+ Substitution On Structural & Optical Parameters And Electrical Behavior On Mg-Zn Ferrites Synthesized Via Co-Precipitation Method, J Supercond Nov Magn 35 (2022) 719–732. Https://Doi.Org/10.1007/S10948-021-06124-1/Figures/15.
[15]. K.R. Desai, S.T. Alone, S.R. Wadgane, S.E. Shirsath, K.M. Batoo, A. Imran, E.H. Raslan, M. Hadi, M.F. Ijaz, R.H. Kadam, X-Ray Diffraction Based Williamson–Hall Analysis And Rietveld Refinement For Strain Mechanism In Mg–Mn Co-Substituted Cdfe2o4 Nanoparticles, Physica B Condens Matter 614 (2021) 413054. Https://Doi.Org/10.1016/J.Physb.2021.413054.
[16]. G. Vinod, K. Rajashekhar, D. Ravinder, J.L. Naik, Structural, Electrical, And Magnetic Properties Of Erbium (Er3+) Substituted Cu–Cd Nano-Ferrites, Journal Of Materials Science: Materials In Electronics 32 (2021) 24069–24082. Https://Doi.Org/10.1007/S10854-021-06869-4.
[17]. G. Vinod, K. Rajashekhar, Y. Sandeep, J. Laxman Naik, Influence Of Re-Gd3+ Ion Substitution On Structure, Morphology, Optical, And Magnetic Analysis Of Cu-Cd Based Nano Ferrites Synthesized By Low-Temperature Citrate Sol–Gel Auto Combustion Method, J Magn Magn Mater 562 (2022) 169772. Https://Doi.Org/10.1016/J.Jmmm.2022.169772.
[18]. K. Rajashekhar, G. Vinod, K. Mahesh Kumar, J.L. Naik, Impact Of Erbium (Er) Doping On The Structural And Magnetic Properties Of Ni-Cu (Ni0.1cu0.9fe2o4) Nanoferrites, J Magn Magn Mater 555 (2022) 169323. Https://Doi.Org/10.1016/J.Jmmm.2022.169323.
[19]. A. Aslam, A.U. Rehman, N. Amin, M. Ajaz Un Nabi, Q. Ul Ain Abdullah, N.A. Morley, M.I. Arshad, H.T. Ali, M. Yusuf, Z. Latif, K. Mehmood, Lanthanum Doped Zn0.5co0.5laxfe2−Xo4 Spinel Ferrites Synthesized Via Co-Precipitation Route To Evaluate Structural, Vibrational, Electrical, Optical, Dielectric, And Thermoelectric Properties, Journal Of Physics And Chemistry Of Solids 154 (2021). Https://Doi.Org/10.1016/J.Jpcs.2021.110080.
[20]. M. Yousaf, M.N. Akhtar, B. Wang, A. Noor, Preparations, Optical, Structural, Conductive And Magnetic Evaluations Of Re's (Pr, Y, Gd, Ho, Yb) Doped Spinel Nanoferrites, Ceram Int 46 (2020) 4280–4288. Https://Doi.Org/10.1016/J.Ceramint.2019.10.149.
[21]. H. Ghorbani, M. Eshraghi, A.A. Sabouri Dodaran, P. Kameli, S. Protasowicki, C. Johnson, D. Vashaee, Effect Of Yb Doping On The Structural And Magnetic Properties Of Cobalt Ferrite Nanoparticles, Mater Res Bull 147 (2022) 111642. Https://Doi.Org/10.1016/J.Materresbull.2021.111642.
[22]. S. Kumari, N. Dhanda, A. Thakur, V. Gupta, S. Singh, R. Kumar, S. Hameed, P. Thakur, Nano Ca–Mg–Zn Ferrites As Tuneable Photocatalyst For Uv Light-Induced Degradation Of Rhodamine B Dye And Antimicrobial Behavior For Water Purification, Ceram Int 49 (2023) 12469–12480. Https://Doi.Org/10.1016/J.Ceramint.2022.12.107.
[23]. A. Aslam, A.U. Rehman, N. Amin, M. Ajaz Un Nabi, Q. Ul Ain Abdullah, N.A. Morley, M.I. Arshad, H.T. Ali, M. Yusuf, Z. Latif, K. Mehmood, Lanthanum Doped Zn0.5co0.5laxfe2−Xo4 Spinel Ferrites Synthesized Via Co-Precipitation Route To Evaluate Structural, Vibrational, Electrical, Optical, Dielectric, And Thermoelectric Properties, Journal Of Physics And Chemistry Of Solids 154 (2021) 110080. Https://Doi.Org/10.1016/J.Jpcs.2021.110080.
[24]. V.A. Lubarda, On The Effective Lattice Parameter Of Binary Alloys, Mechanics Of Materials 35 (2003) 53–68. Https://Doi.Org/10.1016/S0167-6636(02)00196-5.
[25]. S. Taneja, D. Chahar, P. Thakur, A. Thakur, Influence Of Bismuth Doping On Structural, Electrical And Dielectric Properties Of Ni–Zn Nanoferrites, J Alloys Compd 859 (2021) 157760. Https://Doi.Org/10.1016/J.Jallcom.2020.157760.
[26]. P. Thakur, D. Chahar, S. Taneja, N. Bhalla, A. Thakur, A Review On Mnzn Ferrites: Synthesis, Characterization And Applications, Ceram Int 46 (2020) 15740–15763. Https://Doi.Org/10.1016/J.Ceramint.2020.03.287.
[27]. N. Amin, M.S. Ul Hasan, Z. Majeed, Z. Latif, M. Ajaz Un Nabi, K. Mahmood, A. Ali, K. Mehmood, M. Fatima, M. Akhtar, M.I. Arshad, A. Bibi, M.Z. Iqbal, F. Jabeen, N. Bano, Structural, Electrical, Optical And Dielectric Properties Of Yttrium Substituted Cadmium Ferrites Prepared By Co-Precipitation Method, Ceram Int 46 (2020) 20798–20809. Https://Doi.Org/10.1016/J.Ceramint.2020.05.079.
[29]. A.S. Shafaay, R. Ramadan, The Influence Of Zn Doping On The Cation Distribution And Antibacterial Activity Of Cofe2o4, J Supercond Nov Magn 36 (2023) 1465–1480. Https://Doi.Org/10.1007/S10948-023-06589-2/Figures/12.
[30]. S. Ikram, F. Ashraf, M. Alzaid, K. Mahmood, N. Amin, S.A. Haider, Role Of Nature Of Rare Earth Ion Dopants On Structural, Spectral, And Magnetic Properties In Spinel Ferrites, J Supercond Nov Magn 34 (2021) 1745–1751. Https://Doi.Org/10.1007/S10948-020-05723-8.